THE JOURNAL OF PHYSICAL CHEMISTRY B

Article

pubs.acs.org/JPCB

Alkyl Chain Length Dependence of the Dynamics and Structure in the Ionic Regions of Room-Temperature Ionic Liquids

Amr Tamimi, Heather E. Bailey, and Michael D. Fayer*

Department of Chemistry, Stanford University, Stanford, California 94305, United States

Supporting Information

ABSTRACT: The dynamics of four 1-alkyl-3-methylimidazolium bis(trifluoromethylsulfonyl)imide room-temperature ionic liquids (RTILs) with carbon chain lengths of 2, 4, 6, and 10 were studied by measuring the orientational and spectral diffusion dynamics of the vibrational probe $SeCN^-$. Vibrational absorption spectra, two-dimensional infrared (2D IR), and polarization-selective pump−probe (PSPP) experiments were performed on the CN stretch. In addition, optical heterodyne-detected optical Kerr effect (OHD-OKE) experiments were performed on the bulk liquids. The PSPP experiments yielded triexponential anisotropy decays, which were analyzed with the wobbling-in-a-cone model. The slowest decay, the complete orientational randomization, slows with increasing chain length in a hydrodynamic trend consistent with the increasing viscosity. The shortest time scale wobbling motions are insensitive to chain length, while the intermediate time scale wobbling slows mildly as the chain length increases. The 2D IR spectra measured in parallel ($\langle XXXX \rangle$) and perpendicular ($\langle XXYY \rangle$) polarization configurations gave different decays, showing that reorientation-induced spectral diffusion (RISD) contributes to the dynamics. The spectral diffusion caused by the RTIL structural fluctuations was obtained by removing the RISD contributions. The faster structural fluctuations are relatively insensitive to chain length. The slowest structural fluctuations slow substantially when going from Emim (2 carbon chain) to Bmim (4 carbon chain) and slow further, but more gradually, as the chain length is increased. It was shown previously that K^+ causes local ion clustering in the Emim RTIL. The K^+ effect increases with increasing chain length. The OHD-OKE measured complete structural randomization times slow substantially with increasing chain length and are much slower than the dynamics experienced by the $SeCN^-$ located in the ionic regions of the RTILs.

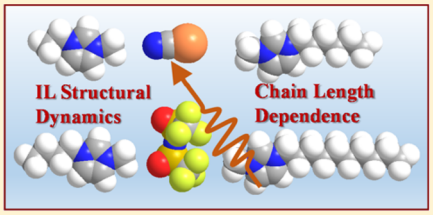

1. INTRODUCTION

Room-temperature ionic liquids (RTILs) have properties that are distinct from other ionic liquids and from common organic liquids. RTILs are liquid at around room temperature, in contrast to, for example, liquid NaCl, which melts at 1074 K. The low melting point of RTILs is typically achieved by using molecular ions, often organic, that are asymmetric, large, have diffuse or delocalized charge, or some combination of these properties. The presence of these properties in the cation, anion, or both prevents crystallization by reducing the enthalpic incentive and/or increasing the entropic cost.[1,2] The vast number of cation and anion combinations results in a wide range of liquids with distinct properties.

One frequently studied class of RTILs has cations based on imidazolium with a methyl substituent on one nitrogen and another longer-chain alkyl substituent on the other nitrogen. These imidazolium cations can be paired with many anions, but their combination with the anion, bis(trifluoromethylsulfonyl)-imide (NTf_2^-), yields especially desirable properties, chemical stability and relatively low viscosities, in particular. We abbreviate the RTILs of the form 1-alkyl-3-methylimidazolium bis(trifluoromethylsulfonyl)imide as $C_n$mimNTf_2, where the subscript n is the number of carbons in the alkyl substituent. These liquids have practical synthesis with ease of functionalization, good chemical stability, and a wide window of electrochemical stability. Along with low viscosities, these properties make them interesting for applications, for example, in batteries.[3]

Increasing the alkyl chain length increases the liquid's viscosity. As the alkyl chain length increases, the liquids organize such that there are distinct ionic and organic regions.[2,4−11] A study of the orientational relaxation of a nonpolar fluorescent probe located in the alkyl regions of $C_n$mimNTf_2 as a function of chain length showed that the hydrodynamic friction experienced by the fluorescent probe approached that of a long-chain liquid hydrocarbon in going from n = 2 (ethyl) to n = 10 (decyl).[11]

In this paper, we present a study of the influence of chain length on the dynamics and structural properties of the ionic regions of $C_n$mimNTf_2 liquids for n = 2, 4, 6, and 10 (ethyl, butyl, hexyl, and decyl) (see Figure 1). We abbreviate the cations in order as $Emim^+$, $Bmim^+$, $Hmim^+$, and $Dmim^+$ and the RTILs correspondingly as EmimNTf_2, BmimNTf_2, HmimNTf_2, and DmimNTf_2. Ultrafast two-dimensional infrared (2D IR) vibrational echoes, polarization-selective pump−probe (PSPP) experiments, and linear absorption FT-IR measurements were performed on the CN stretching mode of the low-concentration selenocyanate anion ($SeCN^-$), which is intro-

Received: May 28, 2016
Revised: July 2, 2016
Published: July 7, 2016

DOI: 10.1021/acs.jpcb.6b05397
J. Phys. Chem. B 2016, 120, 7488−7501

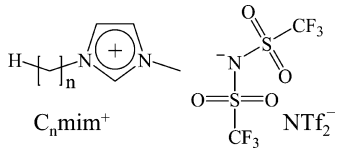

Figure 1. Chemical structure of $C_n$mimNTf_2.

duced into the RTILs as KSeCN. $SeCN^-$ is not soluble in hydrocarbons and thus is located in the ionic regions of the liquids. The CN stretch of $SeCN^-$ has a long vibrational lifetime (>100 ps), which makes it possible to perform the time-dependent experiments over a substantial time range, from less than a picosecond to several hundred picoseconds. Because of its small size relative to the RTIL cation and anion, $SeCN^-$ is unlikely to cause a significant change in the overall liquid structure.

The FT-IR absorption spectra of the CN stretch show a small but measurable peak shift and a slight broadening as the alkyl chain length is increased. The changes in the spectra, though minor, are an indication that the chain length does have some impact on the structure of the ionic regions, resulting in changes in the intermolecular interactions between the $SeCN^-$ vibrational probe and its environment. Infrared PSPP experiments were used to measure the vibrational lifetimes and orientational relaxation (anisotropy decay). The CN stretch lifetimes do not change with chain length. They are all around 105 ps. This long lifetime makes it possible to collect data to ~300 ps. For all samples, the anisotropy decays fit well to triexponential functions. These decays are analyzed with the wobbling-in-a-cone model,[12−18] in which at short times orientational relaxation is confined to a cone of angles. For $SeCN^-$ in the RTILs, the two short time anisotropy decays reflect wobbling in a first cone followed by constraint release that allows an additional range of angles to be sampled within a second cone of restriction. The final slowest decay is caused by diffusive orientational relaxation that completely randomizes the $SeCN^-$ orientations. This picture of orientational sampling, which is restricted by the environment, requiring environmental constraint release to enable additional orientational randomization, is well supported by detailed analysis of simulations in similar systems.[19] Wobbling time constants and cone angles were determined. Wobbling in the first cone shows virtually no dependence on the RTIL chain length. Wobbling in the second cone is mildly dependent on the chain length. The final complete orientational randomization slows substantially as the chain length is increased in a manner that is consistent with the increased viscosity with chain length and a hydrodynamic description of the orientational relaxation. These results provide information on the structural evolution in the ionic regions as a function of chain length.

2D IR spectroscopy measures the structural fluctuations of a system by observing spectral diffusion. This type of spectral diffusion is referred to as structural spectral diffusion (SSD). The results show that the SSD occurs on two time scales. The shorter time scale is independent of the alkyl chain length. The longer time scale displays a substantial slowing in going from Emim to Bmim. As the chain length is increased further, there is additional slowing of the slow SSD component, but to a lesser degree than what occurred in going from Emim to Bmim. For all chain length samples, all of the SSD, that is, the sampling of liquid structures that contribute to inhomogeneous broadening, is fast compared to the time scales for complete orientational randomization of the samples as measured using optical heterodyne-detected optical Kerr effect (OHD-OKE) experiments.

In the PSPP and 2D IR measurements, the experimental time window is limited by the CN vibrational lifetime (~100 ps). Within this time window, the data do not decay to zero but rather to a small offset. This offset has been examined in detail previously for the system of KSeCN in EmimNTf_2. It is caused by anion and cation clustering around the K^+. $SeCN^-$ anions that are in such clusters undergo much slower dynamics, giving rise to the offset in the data. It was found that the size of the offset increased as the alkyl chain length was increased.

2. EXPERIMENTAL DATA ANALYSIS PROCEDURES

2.A. PSPP Spectroscopy. Both PSPP and 2D IR measurements were performed with pump−probe geometry using the same optical platform. Details of the setup have been reported previously;[20] here a brief description is presented. A home-built mid-IR optical parametric amplifier, which was pumped by a Ti:sapphire regenerative amplifier, produced ~170 fs pulses centered at 2075 cm^{-1} with ~8 μJ pulse energy. The mid-IR pulses were split into a weaker probe pulse and a stronger pump pulse. The weak pulse was routed through a mechanical delay line that was used to set the waiting time T_w for the 2D IR experiments (see below) and the delay time in the PSPP experiments. The strong pulse was sent to an acousto-optic mid-IR Fourier-domain pulse shaper. The output beam from the pulse shaper, which generated pulses 1 and 2 in the 2D IR experiments and the single pump pulse in the PSPP experiments, was crossed in the sample with the probe pulse. The probe pulse, which carried the signal in pump−probe and vibrational echo experiments, was sent to a spectrometer equipped with a 32 element HgCdTe (MCT) IR array detector. In the 2D IR experiments, the pulse shaper was used to make two of the three excitation pulses (1 and 2) and control their delay and phase (phase cycling). In the PSPP experiments, the pulse shaper was used to chop the pump pulse and for phase cycling. In both experiments, the phase cycling removed scattered light from the pump that could interfere with measurements of small signals in the probe direction.

The method for acquiring the PSPP spectra was optimized to ensure that the parallel and perpendicular polarization configurations were acquired with the same experimental conditions. The probe polarization was fixed horizontal (in the plane of the optical table), with an extra polarizer (wire-grid polarizer, ISP Optics) before the last mirror preceding the sample to eliminate any depolarization effects from the preceding optics and delay line retroreflector. The pump beam polarization was changed from horizontal to 45° relative to the probe using a half-wave plate and polarizer. The polarizer was placed immediately before the sample to eliminate any depolarization. Directly after the sample, the probe was resolved using a polarizer mounted in an automated rotation stage that alternated between +45 and −45° relative to the probe polarization. Because the pump polarization was +45°, these correspond to the parallel and perpendicular configurations, respectively. The pump and probe were not changed before the sample in making the two polarization measurements. Because the response of the spectrometer grating is polarization-dependent, another polarizer was placed right before the entrance slit and set to horizontal polarization. This guaranteed unbiased detection of both polarization pathways.

DOI: 10.1021/acs.jpcb.6b05397
J. Phys. Chem. B 2016, 120, 7488−7501

The principal 2D IR data analysis did not rely on being able to add or subtract spectra from different polarization configurations. Signal-to-noise was, therefore, prioritized, and a different scheme for controlling the polarization was employed in performing the polarized 2D IR measurements. The probe was kept horizontal as in the PSPP experiments, but instead of pumping at 45°, we pumped at 0 and 90° for the ⟨XXXX⟩ and ⟨XXYY⟩ pathways, respectively. The resolving polarizer immediately after the sample was kept horizontal and was not changed. Because recovering isotropic spectra (discussed below) requires the ability to add spectra, comparison with the corresponding PSPP experiments was used to ensure the correct relative amplitudes.

PSPP spectroscopy measures the vibrational lifetime and the anisotropy, which is proportional to the second-order Legendre polynomial orientational correlation function, $C_2(t)$.[21] The form of this correlation function is known for diffusive orientational dynamics as well as for various restricted diffusion models (wobbling-in-a-cone).[13,14,17,18] The analysis of the anisotropy has been extensively employed in developing an understanding of the orientational dynamics of molecular probes.[15,16,22,23]

In measuring the anisotropy, two configurations where the pump and probe have parallel and perpendicular polarizations were acquired. For third-order pump−probe spectroscopy, the orientational contribution to any polarization configuration is given by the following equations, where the parallel and perpendicular signals are $S_{\parallel}(t)$ and $S_{\perp}(t)$, respectively. The population lifetime decay is $P(t)$.[21]

$$S_{\parallel} = P(t)[1 + 0.8C_2(t)] \tag{1}$$

$$S_{\perp} = P(t)[1 - 0.4C_2(t)] \tag{2}$$

From these two experimental configurations, the following two observables can be extracted

$$P(t) = \frac{[S_{\parallel}(t) + 2S_{\perp}(t)]}{3} \tag{3}$$

$$r(t) = \frac{S_{\parallel}(t) - S_{\perp}(t)}{S_{\parallel}(t) + 2S_{\perp}(t)} \tag{4}$$

where $r(t)$ is the anisotropy, defined as $r(t) = 0.4C_2(t)$.

For an anisotropy decay that is a single exponential, a common physical model is a single orientational diffusion process. An initial deviation from 0.4 at very short time is caused by the ultrafast inertial orientational motions.[22] The inertial drop is too fast to measure. However, frequently the anisotropy decay is not a single exponential. A multiexponential can be described in terms of a hierarchy of diffusive processes, each limited to an angular cone with a certain half angle. The angular limitation is imposed by a local interaction. As the solvent structures randomize, the entire cone reorients on a slower time scale.

An orientational correlation function under restricted reorientation does not decay to zero but to a level determined by the extent of orientational space that remains unsampled. $C_2(t)$ decays to the square of an order parameter Q.[17,18] Explicitly including the wobbling-in-a-cone model with a single cone

$$Q^2 = \left(\frac{1}{2}\cos\theta_0(1 + \cos\theta_0)\right)^2 \tag{5}$$

where θ_0 is the half-angle of the cone.[13,14,17,18] Including the final complete diffusive orientational randomization yields[15]

$$C_2(t) = (Q^2 + (1 - Q^2)\exp(-t/\tau_c))\exp(-t/\tau_m) \tag{6}$$

where τ_c is the time constant for the restricted diffusion in the cone and τ_m is the time constant for the final complete orientational randomization.

As the anisotropies measured here are triexponentials with an initial inertial drop, an inertial cone and two diffusive cones are included in addition to the final free diffusion. The resulting form for $C_2(t)$, which is used in fitting the anisotropy curves, is[16]

$$\begin{aligned} C_2(t) = {} & (T^2 + (1 - T^2)\exp(-t/\tau_{in})) \\ & \times (S^2 + (1 - S^2)\exp(-t/\tau_{c1})) \\ & \times (R^2 + (1 - R^2)\exp(-t/\tau_{c2}))\exp(-t/\tau_m) \end{aligned} \tag{7}$$

where T, S, and R are the order parameters for the inertial and two diffusive cones, respectively, and τ_{in}, the time constant for the inertial cone, is taken to be much faster than our time resolution. The size of the inertial cone is reflected in the initial value of the anisotropy when the experimental curve is extrapolated a few hundred femtoseconds back to $t = 0$.

2.B. 2D IR Spectroscopy. The CN stretch absorption band of $SeCN^-$ in the RTILs is inhomogeneously broadened because the $SeCN^-$ experiences a variety of liquid structures. The different liquid structures shift the absorption frequency of the CN mode. At an instant in time, an individual $SeCN^-$ will experience a particular liquid environment that will give rise to an absorption frequency within the range of frequencies in the inhomogeneous line. However, the liquid structure is not static but evolves with time. The change in structure experienced by a molecule will cause its frequency to change. The time evolution of the frequency is spectral diffusion. Then, measuring the time dependence of the frequency yields a determination of the time evolution of the liquid structure. This type of spectral diffusion is the SSD.

In a 2D IR experiment, a series of 2D spectra are acquired with increasing time for the liquid structure to evolve.[24] As the time is increased, the shape of the 2D band changes shape. The spectral diffusion time dependence is determined from the time-dependent shape of the 2D band. In the 2D IR experiment, three pulses impinge on the sample. Nonlinear radiation field−matter interactions give rise to a fourth pulse, the vibrational echo. The experiments are conducted with two polarization configurations. In one configuration, all of the pulses (three input pulses and the echo pulse) have the same polarization, ⟨XXXX⟩. In the other configuration considered here, the first two pulses have a polarization that is perpendicular to the third pule and the echo pulse, ⟨XXYY⟩. In the experiments on $SeCN^-$, it was found that the decays for the two polarizations differed. The difference demonstrates that, aside from SSD, there is an additional source of spectral diffusion, namely, reorientation-induced spectral diffusion (RISD).[25,26] RISD is caused by the orientational motions of the vibrational probe, $SeCN^-$. The total spectral diffusion observed in the experiments is a combination of SSD and RISD.[25,26] Because the orientational relaxation dynamics are known from the PSPP experiments, the SSD and RISD contributions to the spectral diffusion can be separated, and the SSD, which reflects the dynamics of interest, is obtained.[25]

DOI: 10.1021/acs.jpcb.6b05397
J. Phys. Chem. B 2016, 120, 7488−7501

In a 2D IR experiment,[27] the time between pulses 1 and 2 is τ, and the time between pulses 2 and 3 is T_w. The vibrational echo pulse is emitted after pulse 3. The two pump pulses (1 and 2) label all of the vibrational oscillators with their initial frequencies. During the time period T_w, the frequencies of the vibrational oscillators evolve because of both SSD and RISD. Then pulse 3 generates the vibrational echo signal that reads out the frequencies of the vibrational oscillators after the system has had the period T_w to evolve. The vibrational echo signal propagates collinearly with pulse 3, which serves as the local oscillator (LO) to detect the phase of the echo signal.

The 2D IR spectra require two Fourier transforms to go from the time domain to the frequency domain. The spectrograph performs one of the Fourier transforms experimentally by resolving the echo/LO pulse into its composite frequencies giving the ω_m (vertical axis) of the 2D spectrum. The horizontal axis, ω_τ, is obtained by scanning τ. When τ is scanned, the echo moves in phase relative to the fixed LO, producing an interferogram. The interferogram, recorded at each ω_m, is numerically Fourier transformed to give the ω_τ axis of the 2D spectrum

For each T_w, τ is scanned and a 2D IR spectrum is obtained. The spectral diffusion (combined SSD and RISD) is extracted from the evolution of the 2D band shape at each T_w. At short T_w, the detection frequency (ω_m) is approximately the same as the excitation frequency (ω_τ), giving a spectrum that is elongated along the diagonal (upper right to lower left corners of the 2D spectrum). The shape of the spectrum becomes closer to round as spectral diffusion progresses, which causes the initial and final frequencies to be less correlated. The spectrum will be completely round when all structures have been sampled during the period T_w.

The results of the 2D IR experiments are analyzed in terms of the frequency−frequency correlation function (FFCF), which quantifies the spectral diffusion in terms of the frequency fluctuation amplitudes and time constants. The FFCF is the probability that a vibration with an initial frequency in the inhomogeneous spectral distribution still has the same frequency at a later time, averaged over all initial frequencies. To extract the FFCF from the 2D spectra, the center line slope (CLS) analysis was employed.[28,29] The CLS is a function of T_w, CLS(T_w), and has been shown to be equal to the normalized FFCF. At each T_w, the slope of the center line is determined, and these CLS values form CLS(T_w). The FFCF was modeled with a simplified Kubo form, given by

$$C_{tot}(t) = \langle \delta\omega(t)\delta\omega(0)\rangle = \sum_i \Delta_i^2 \exp(-t/\tau_i) \tag{8}$$

Here, $\delta\omega(t) = \omega(t) - \langle\omega\rangle$ is the instantaneous frequency fluctuation with $\langle\omega\rangle$, the average frequency. Δ_i is the frequency fluctuation amplitude of each component, and τ_i is its associated time constant. A fit to the CLS(T_w) vs T_w curve, which is the normalized FFCF, gives spectral diffusion time constants and amplitude factors. A component of the FFCF with $\Delta_i\tau_i \ll 1$ is motionally narrowed. When a component is motionally narrowed, Δ and τ cannot be determined separately. The motionally narrowed homogeneous contribution to the absorption spectrum has a pure dephasing line width given by $\Gamma^* = \Delta^2\tau/\pi = 1/\pi T_2^*$, where T_2^* is the pure dephasing time. The observed homogeneous dephasing time, T_2, also has contributions from the vibrational lifetime and orientational relaxation

$$\frac{1}{T_2} = \frac{1}{T_2^*} + \frac{1}{2T_1} + \frac{1}{3T_{or}} \tag{9}$$

where T_2^*, T_1, and T_{or} are the pure dephasing time, vibrational lifetime, and orientational relaxation times, respectively. The total homogeneous line width is $\Gamma = 1/\pi\ T_2$. The total homogeneous dephasing time T_2 and the values of Δ_i in units of frequency are obtained from the experimental data by a simultaneous fit to the CLS decay and the experimental linear absorption line shape.[28]

2.C. RISD. As discussed in the Introduction, the total FFCF, $C_{tot}(t)$, can have contributions from both SSD and RISD. To assess the extent of the RISD contribution, one measures CLS(T_w) in both the parallel ($\langle$XXXX$\rangle$) and perpendicular ($\langle$XXYY$\rangle$) 2D IR polarization configurations. If the CLS(T_w) decays are identical with these two configurations, then there is no RISD. As shown in the 2D IR data below, the parallel and perpendicular CLS(T_w) are different, and therefore, RISD must be taken into account in analyzing the data to extract the SSD, which reflects the structural evolution of the IL.

For first-order Stark effect coupling or any vector coupling that is first-order in the interaction that determines the probe frequency, the total FFCF, $C_{tot}(t)$, has been shown to have the form

$$C_{tot}^i(t) = F_{SSD}(t)R_i(t) \tag{10}$$

where $F_{SSD}(t)$ is the structural contribution to the FFCF, which is caused by fluctuations in the liquid structure, and $R_i(t)$ is the RISD contribution, where i is parallel, perpendicular, or isotropic (see below).[25,26] The second term, $R_i(t)$, captures the effect of the probe dipole reorientation on the spectral fluctuations including polarization weighting to account for the experimental geometry. The normalized RISD contribution for the parallel case is

$$R_{para}(t) = \frac{3}{25}\left[\frac{11C_1(t) + 4C_3(t)}{1 + 0.8C_2(t)}\right] \tag{11}$$

and that for the perpendicular case is

$$R_{perp}(t) = \frac{3}{25}\left[\frac{7C_1(t) - 2C_3(t)}{1 - 0.4C_2(t)}\right] \tag{12}$$

where $C_1(t)$, $C_2(t)$, and $C_3(t)$ are the first-, second-, and third-order Legendre polynomial orientational correlation functions, respectively.[25,26] It is important to point out that there are no adjustable parameters in eqs 11 and 12. $C_2(t)$ is measured using the PPSP experiments. Once $C_2(t)$ is known from the experiments, $C_1(t)$ and $C_3(t)$ are obtained from relations derived previously that relate them to $C_2(t)$.[25] The relations include the wobbling-in-a-cone and the complete final diffusive randomization.

In the experiments, $C_{tot}^{para} = F_{SSD}(t)R_{para}(t)$ and $C_{tot}^{perp} = F_{SSD}(t)R_{perp}(t)$ are measured. The two CLS(T_w) decay curves are fit simultaneously. The adjustable parameters are in the structural part of the FFCF, $F_{SSD}(t)$. $F_{SSD}(t)$ is the same in the parallel and perpendicular 2D IR data. While $C_{tot}^{para}(t)$ and $C_{tot}^{perp}(t)$ are the direct experimental observables, there is another quantity that is useful. Simulations of 2D IR data, in general, do not include polarized radiation fields. Simulations calculate $C_{tot}^{iso}(t)$, where iso stands for isotropic

$$C_{tot}^{iso}(t) = F_{SSD}(t)R_{iso}(t) \tag{13}$$

DOI: 10.1021/acs.jpcb.6b05397
J. Phys. Chem. B 2016, 120, 7488−7501

where $R_{iso}(t) = C_1(t)$.[26] As discussed below, $C_{tot}^{iso}(t)$ is obtained by adding the parallel 2D IR spectrum to twice the perpendicular 2D IR spectrum with the proper scaling at each T_w. The CLS method is then used on the resulting added spectra to obtain the normalized isotropic FFCF. It is important to note that the isotropic FFCF still has contributions from reorientation, RISD, and SSD. $F_{SSD}(t)$ is the same in the parallel, perpendicular, and isotropic FFCFs.

2.D. OHD-OKE Spectroscopy. The OHD-OKE experiment is a nonresonant spectroscopic technique in which a linearly polarized pump pulse induces a transient birefringence in a sample. The time decay of the birefringence (related to the orientational relaxation) is measured by a physically delayed probe pulse, polarized at 45° relative to the pump. Birefringence induced by the pump pulse causes an ellipticity in the probe pulse that is measured after a crossed polarizer.[30,31] The signal decays with time as the birefringence is reduced by orientational relaxation. The signal is the derivative of the polarizability−polarizability correlation function, which is the same as the derivative of the orientational relaxation correlation function (second Legendre polynomial correlation function) at all but very short times where interaction-induced (collision-induced) contributions may influence the signal.[32,33]

The details of the OHD-OKE setup have been described in detail previously.[34] Briefly, a Ti:sapphire oscillator/regenerative amplifier produces pulses at 5 kHz repetition rate with energy up to 300 μJ/pulse and pulse widths that are varied from 60 fs to 125 ps depending on the time scale being studied. Because of the nonresonant nature of this experiment, the pulses can be chirped to change their duration without affecting the measured dynamics. The regenerative amplifier output is beam split into the pump and probe beams.

The signal is heterodyned to improve the signal-to-noise and to permit a phase cycling pulse sequence. The data are taken with a four-shot sequence in which the phase of the probe heterodyne field and the pump polarization are cycled.[34,35] Data are obtained with a balanced detector and a lock-in amplifier. For the data taken at long time, the probe pulse and delay line are replaced with a CW probe beam, and a 1 ns digitizer is employed to record the data. Data can be collected from hundreds of femtoseconds to microseconds.

Here, we are interested in the slowest time scale of the OHD-OKE decays, which reflect the final complete orientational randomization of the sample. In many types of liquids,[36] RTILs,[34,37] supercooled liquids,[38,39] and nematogens in the isotropic phase of liquid crystals,[38,40] the final exponential decay of the data is proceeded by two power law decays. To extract the final exponential decay, a global fit was performed using the fitting function

$$F(t) = [pt^{-z} + dt^{b-1}]e^{-t/t} \quad (14)$$

which is based on schematic mode coupling theory.[37−39] The power laws describe the early time non-Markovian caged dynamics prior to a final exponential decay, which is the complete orientational randomization.

2.E. Sample Preparation. Four samples were used in this study, that is, $EmimNTf_2$, $BmimNTf_2$, $HmimNTf_2$, and $DmimNTf_2$, with KSeCN added as the vibrational probe. KSeCN (Acros) and the four RTILs (Iolitec) were purchased from commercial sources and used after extended drying under vacuum and moderate heating (~100 mTorr and ~65 °C). The amount of water in the dried RTILs was characterized by coulometric Karl Fischer titration (Mettler Toledo) and found to be under 10 ppm. After drying, the materials were stored in a nitrogen-atmosphere glovebox. Solutions were prepared in the glovebox gravimetrically. KSeCN was added at a molar ratio of 1:200 ion pairs per $C_n mimNTf_2$ ion pair. The samples were filtered with a 0.02 μm filter (Whatman Anotop) in the glovebox.

The RTIL solutions were placed into a 1 cm path length cuvette for the OKE experiments. For the IR experiments, the solutions were sandwiched between 1 in. diameter calcium fluoride windows with a polytetrafluoroethylene ring spacer to determine the sample path length. These sample cells are assembled in the glovebox and then placed in the infrared spectrometry setup with an ambient temperature of 295 K.

Before and after the ultrafast infrared experiments were conducted, linear Fourier transform infrared (FT-IR) spectra of the samples were collected to ensure that no appreciable sample degradation had taken place and no water had been picked up during the experiments. Linear spectra were also collected for each RTIL without the KSeCN vibrational probe, which were used for background subtraction in the linear FT-IR spectra.

3. RESULTS AND DISCUSSION

3.A. Linear Infrared Spectra. The linear FT-IR spectra of the CN stretch of $SeCN^-$ in the four RTILs are shown in Figure 2. The spectra are background-subtracted and normalized to facilitate comparison. There is a small band at ~2020 cm^{-1} that remained after background subtraction. It was excluded when fitting the main bands. The four peaks were individually fit to a Voigt profile, starting from at 25% amplitude on the red side to avoid the background band to 2132 cm^{-1} on the blue. The fit over this range has a coefficient of determination of $R^2 > 0.9999$ for all four curves. The results of these fits are given in Table 1.

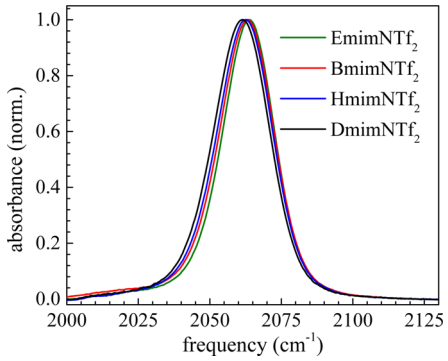

Figure 2. Background-subtracted and normalized FT-IR spectra of the CN stretch of $SeCN^-$ in four ILs: $EmimNTf_2$, $BmimNTf_2$, $HmimNTf_2$, and $DmimNTf_2$. The spectra exhibit slight broadening and shift to the red as the length of the cation alkyl chain increases.

The partitioning into a Gaussian and Lorentzian component that results from the Voigt fit can only yield qualitative conclusions regarding the nature of the broadening. The numbers are nevertheless reported as a phenomenological description of the experimental line shapes. The peak positions and resulting total fwhm are quantitative, however, and display a mild trend. As the chain length increases, the center shifts slightly to the red and the width increases slightly.

As we have discussed in previous work,[41,42] the resonance frequency of the CN stretch of the $SeCN^-$ anion depends on its

DOI: 10.1021/acs.jpcb.6b05397
J. Phys. Chem. B 2016, 120, 7488−7501

Table 1. Voigt Fit Results for the Linear FT-IR Spectra[a]

	center (cm^{-1})	w_G (cm^{-1})	w_L (cm^{-1})	w_V (cm^{-1})
$EmimNTf_2$	2063.69 ± 0.01	17.60 ± 0.05	6.02 ± 0.07	21.0
$BmimNTf_2$	2063.06 ± 0.01	18.76 ± 0.05	5.68 ± 0.07	22.0
$HmimNTf_2$	2062.41 ± 0.01	19.35 ± 0.05	5.35 ± 0.07	22.4
$DmimNTf_2$	2061.29 ± 0.01	19.85 ± 0.05	5.13 ± 0.07	22.7

[a]The Lorentzian and Gaussian contributions to the total Voigt fwhm, w_V,[57] are reported as w_G and w_L. Errors reported are standard errors of the fit.

interactions with the surrounding solvent environment. In strongly interacting environments such as bulk water, the absorption is blue-shifted, whereas it is comparatively red-shifted in very small reverse micelles where the $SeCN^-$ interacts predominantly with the sulfonate head groups.[42] Because the solvation environment in the RTILs is ionic, the similarity of the center frequencies reported in Table 1 to the smallest reverse micelle case (~2065 cm^{-1}) is consistent with the ionic nature of the environment. Compared with the smallest reverse micelle, however, the RTIL peaks are all broader and more red-shifted, with this trend increasing with alkyl chain length. This is consistent with the relatively disordered RTIL having a broader range of environments than the ordered nature of a reverse micelle. The broadening shown in Figure 2 as the chain length increase is taken suggests increased heterogeneity, that is, there is a broader range of possible ion-packing structures for the longer chains. The longer-chain RTILs have increased polar−apolar ordering,[9,43,44] which produces structures in the ionic regions that do not occur for shorter chain lengths. Concomitantly, these additional structures may produce looser ion packing that is manifested as an overall red shift of the spectra.

3.B. Time-Resolved Measurements. *3.B.1. PSPP.* The acquired PSPP curves for all four chain lengths are processed according to eqs 3 and 4 to yield the isotropic decay curve $P(t)$ and the anisotropy $r(t)$. $P(t)$ is the excited-state population decay in the absence of other processes. In particular, nonuniform pumping across the spectral band caused by the non-Condon effect (the transition dipole varies across the band) or nonuniform background absorption will result in spectral diffusion affecting the population dynamics at a particular wavelength, and $P(t)$ will not be a single-exponential decay. This nonexponential behavior has been discussed previously for $SeCN^-$ in water.[42] The $P(t)$ curves (not shown) generally display some deviation from single-exponential behavior at short time. Therefore, to determine the actual vibrational lifetime, the data were fit starting a longer times at which the decays are single-exponential. Changing the start point of the fit from 100 to 200 ps and fitting out to 300 ps changes the numbers only a few picoseconds out of ~105 ps. For any fit, the different chain lengths are within 2 ps of each other. Accounting for spectral diffusion by incorporating two shorter exponential time scales derived from the isotropic CLS fits (see below) improves the quality of the fit over the entire time range and yields values of 105 ± 2 ps for all chain lengths with no trend. Therefore, within experimental error, the CN stretch vibrational lifetime is independent of chain length.

The almost identical lifetimes across the four chain lengths suggest that the environment that the probe experiences in the four RTILs is not significantly different in terms of the coupling to the environment that can influence vibrational relaxation. This is consistent with the similarity among the absorption spectra shown in Figure 2. More broadly, the $SeCN^-$ in all four liquids is surrounded by ions, mainly cations, and thus, no new fundamental interactions arise with growing alkyl chain length. The changing viscosity, growing ordering in the alkyl regions, and the changes in local structure around the probe indicated by the small changes in the absorption do not influence the vibrational relaxation pathways within experimental error.

The anisotropy decays for the four chain lengths are shown in Figure 3. In contrast to the lifetimes, a clear trend is

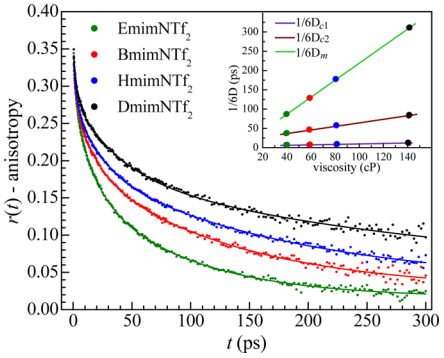

Figure 3. Anisotropy decays of $SeCN^-$ for all four chain lengths are shown (points) with the fits (solid curves) using eq 15. The parameters derived from the fits are given in Table 2. The inset shows the two diffusion constants corresponding to the restricted wobbling-in-a-cone diffusion times reported as $1/6D_{c1}$ and $1/6D_{c2}$ and the final complete randomization, $1/6D_m$. The three diffusion constants all slow down with increasing chain length, but only the final free diffusion slows down to the extent predicted by hydrodynamics.

observed; the anisotropy decays slow down with increasing alkyl chain length. As discussed in section 2.B, the anisotropies can be fit to triexponential functions. The intercept at $t = 0$ is less than 0.4, the maximum possible value. The multi-exponential nature of the decays is caused by constraints on free reorientation, for example, wobbling-in-a-cone. Associated with each angular constraint are both the range of angles sampled and the time scale of the angular sampling. These constraints are overcome at characteristic time scales and thus form a hierarchy of successively greater ranges of sampled orientational space.[16] The ultrafast drop from 0.4, which is not resolved, is caused by inertial motion.

As discussed in section 2.B, in the wobbling-in-a-cone model, each dynamical process has an order parameter and a diffusion constant. The inertial reorientation is dealt with by assigning it an infinitely large diffusion constant so that it samples its full angular cone before the time scales that we consider. The final diffusive motion samples the entire orientational space and thus has an order parameter of zero. With the inertial decay approximated as an instantaneous drop, the fitting formula for $r(t)$ based on eq 7 becomes

$$r(t) = 0.4(T^2)(S^2 + (1 - S^2)\exp(-t/\tau_{c1})) \times (R^2 + (1 - R^2)\exp(-t/\tau_{c2}))\exp(-t/\tau_m) \quad (15)$$

where, as before, T, S, and R are the inertial, first diffusive, and second diffusive cone order parameters and τ_{c1}, τ_{c2}, and τ_m are the first cone diffusive, second cone diffusive, and free diffusive time constants.

In previous work on $EmimNTf_2$,[41] the free diffusive time constant was found to be consistent with the Debye−Stokes−

DOI: 10.1021/acs.jpcb.6b05397
J. Phys. Chem. B 2016, 120, 7488−7501

Table 2. Wobbling-in-a-Cone Parameters

sample	θ_{in}[a]	θ_{c1}[b]	θ_{c2}[b]	θ_{tot}[c]	τ_{c1}(ps)[d]	τ_{c2}(ps)[d]	τ_{m}(ps)[d]	$1/6D_{c1}$[e]	$1/6D_{c2}$[e]	$y_0 \times 10^3$[f]
Emim	16 ± 1	23.0 ± 0.5	33.1 ± 1	43.3 ± 0.4	2.1 ± 0.3	19 ± 2	87 ± 4	8 ± 1	37 ± 3	16 ± 1
Bmim	17 ± 1	22.5 ± 0.5	29.4 ± 1	41.5 ± 0.4	2.0 ± 0.3	20 ± 2	129 ± 7	8 ± 1	47 ± 4	26 ± 1
Hmim	18 ± 1	22.6 ± 0.5	30.2 ± 1	42.7 ± 0.4	2.2 ± 0.3	25 ± 2	178	9 ± 1	57 ± 4	33 ± 2
Dmim	18 ± 1	23.0 ± 0.5	33.6 ± 2	45.9 ± 0.4	3.1 ± 0.3	44 ± 3	311	12 ± 1	82 ± 7	45 ± 6

[a]The inertial cone angle scaled to account for the K^+ induced offset; see the Supporting Information. [b]θ_{c1} and θ_{c2} are the first and second diffusive cone half angles. [c]θ_{tot} is the total cone half angle accounting for all three cones. [d]τ_{c1}, τ_{c2}, and τ_m are the first diffusive cone decay time, the second diffusive cone decay time, and the final free diffusive decay time. [e]D_{c1} and D_{c2} are the first and second cone diffusion constants [f]y_0 is the offset times 10^3.

Einstein (DSE) prediction for slip boundary conditions.[45−47] The DSE prediction for the orientational diffusion constant is given by

$$D = \frac{kT}{\eta V_{eff} \lambda} \tag{16}$$

where k is the Boltzmann constant, η is the viscosity, and λ is a unitless "shape" parameter, tabulated as a function of the axis ratio for the approximate ellipsoid that describes the probe.[48]

In fitting the anisotropies in Figure 3, another effect must be taken into account, that is, the existence of an offset in the data caused by the presence of the potassium counterion. As discussed in detail previously,[41] the presence of the potassium ion at a concentration of 1:200 potassium ions to $C_n$mimNTf$_2$ ion pairs results in a small ensemble of $SeCN^-$ molecules that exhibit dynamics much slower than the majority of $SeCN^-$ ions, which are unaffected by the presence of the potassium. This was verified in the case of EmimNTf$_2$ by performing the same experiments with a native $Emim^+$ counterion as opposed to the K^+, where the offset in the anisotropy all but disappeared, leaving all other numbers unchanged. In addition, increasing the K^+ concentration increased the offset.[41] These results are consistent with the presence of a small ensemble associated with K^+ that has much slower orientational relaxation than the main ensemble. The orientational relaxation for this subset of $SeCN^-$ is so slow that it falls outside of the experimental window set by the vibrational lifetime and appears as an offset in the anisotropy decays of the main ensemble.

Given these previous results on the effect of K^+, all four curves are fit with a triexponential form with an offset. The presence of a free offset creates an unintended issue due to the finite vibrational lifetime. Because the anisotropies are not taken past 300 ps and because the slowest anisotropy component for the two longer-chain RTILs does not decay to zero by 300 ps, a completely free fit cannot resolve the difference between the slowest time scale of the main ensemble and the free offset needed to accommodate the presence of the potassium-influenced ensemble. The results of the completely free triexponential fits are given in the Supporting Information. In EmimNTf$_2$ and BmimNTf$_2$, the decays are fast enough that the offset can be determined and the anisotropy decays can be fit without ambiguity. Previously, the size and shape of $SeCN^-$ were modeled using electronic structure calculations.[41] Fits to the anisotropy decay in EmimNTf$_2$ showed that the slowest component was in agreement with hydrodynamic predictions using slip boundary conditions (see eq 16).[41] Here, the fit to the slowest component of the anisotropy decay in BmimNTf$_2$ again gave the slowest component, in agreement with hydrodynamic predictions for slip boundary conditions using the size and shape parameters determined previously. The ratio of the slowest decays in EmimNTf$_2$ and BmimNTf$_2$ exactly matched the ratio of the RTIL viscosities.

Therefore, it is reasonable to assume that this trend continues for HmimNTf$_2$ and DmimNTf$_2$. The slowest anisotropy decay components (free diffusion decay constant) was set equal to the hydrodynamic prediction using the ratio of the viscosities. Because viscosities depend on water and halide impurities,[49] the temperature-dependent viscosities were measured for the RTILs considered here, which were purchased from the same supplier (Iolitec) as well as dried and handled according to the same procedures. The details of the measurements and the resulting numbers are included in the Supporting Information. Because the temperature dependence was fit well by an Arrhenius form,[50] we used this fit to the temperature dependence of the viscosities to obtain the viscosity at the experimental temperature of 72 °F (295.4 K). This procedure allowed us to fix the $C_2(t)$ free diffusion constant, $\tau_m = 1/6D_m$, where D_m is the diffusion constant for the free diffusion process calculated according to eq 16 by scaling for the viscosity change for HmimNTf$_2$ and DmimNTf$_2$.

With τ_m fixed to the hydrodynamic prediction for the HmimNTf$_2$ and DmimNTf$_2$ samples, the K^+-induced offset can be determined for all four samples. Using EmimSeCN in DmimNTf$_2$ (no K^+) shows a great reduction in the offset, supporting the attribution of the offset to the presence of potassium. The offset increases with chain length. The increase in offset suggests an increase in the population of potassium-affected $SeCN^-$ probes. This is consistent with the offset increase seen in the CLS curves discussed in the next section. The influence of K^+ will be discussed further below.

The results of the analysis of the anisotropy data from fits to eq 15 are given in Table 2. The numbers in Table 2 are the diffusive cone angles and decay times, as well as the total cone angle and the two cone diffusion constants. The wobbling-in-a-cone diffusion constants are determined by both the decay time and the cone angle.[13] None of the diffusive cone angles or time scales are affected by the presence of the offset. The inertial cone angle, however, is affected in a manner discussed in detail in the Supporting Information. As can be seen in Table 2, there is no discernible trend in the two angles and even in the total cone angle, which describes the total cone that is sampled prior to complete orientational relaxation. The cone angles can be understood to represent physical restrictions on reorientation imposed by the solvation environment, which is probably dominated by the imidazolium portion of the cations. Because the physical restrictions are determined by the structure of the solvation shell, the lack of chain length dependence of the cone angles reflects the similarity of the packing of the solvation shell across the four chain lengths. This conclusion is supported by the similarity of the FT-IR spectra and the vibrational lifetimes,

DOI: 10.1021/acs.jpcb.6b05397
J. Phys. Chem. B 2016, 120, 7488−7501

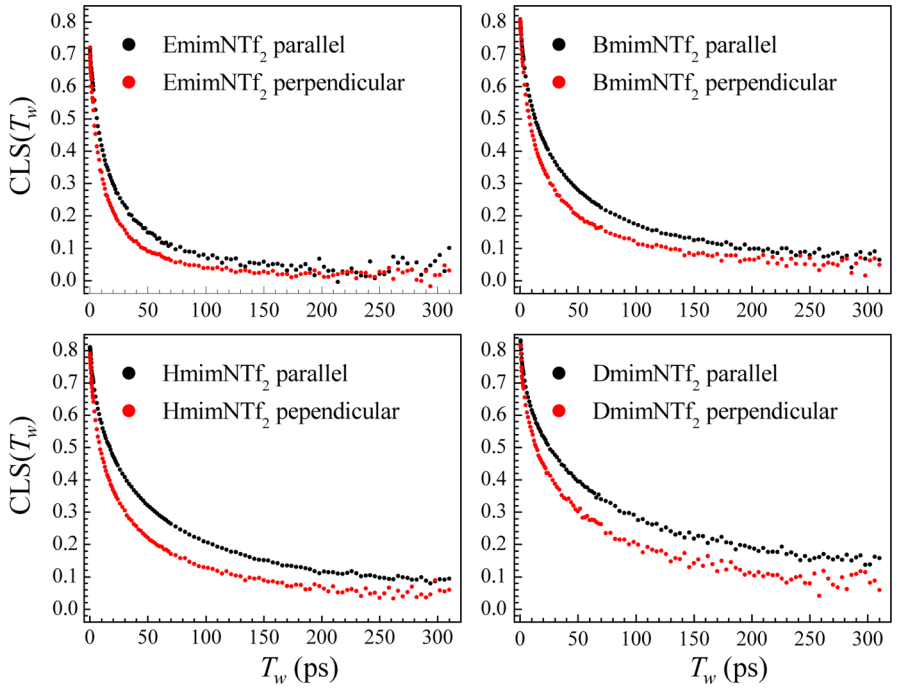

Figure 4. CLS decay curves resulting from experiments in both the parallel and perpendicular polarization configurations for all chain lengths.

all indicators of the immediate chemical environment and its structure.

Because the restriction on orientational motion is imposed by the local solvation structure, the rate at which a restriction is overcome is determined by the time for the restriction to give way through the fluctuations of the surrounding solvation structure. This time determines the next time scale in the hierarchy of angular relaxation processes. Table 2 gives the decay times for both the first and second restricted diffusion, as well as the slowest decay time, which is the diffusive complete orientational randomization. Table 2 also displays the diffusion constants associated with the two cone diffusions. These are calculated from the wobbling-in-a-cone model for a given cone angle and associated decay time[13] and reported as diffusion times for ease of comparison to the complete relaxation diffusion time. The diffusion-constant-derived times are also plotted against the bulk viscosity in the inset of Figure 3. For the first wobbling motion, which is the motion corresponding to the probe overcoming its inertial cone, there is very little slowing down up to $HmimNTf_2$, at which point there is a slight slowing going to $DmimNTf_2$. Because this is a much smaller effect than the viscosity change or the growth of the cation chain length, we deduce that motions involved in this relaxation on the part of the cation are so small in scale that they are mostly insensitive to the presence of the alkyl chain or the increase in the bulk viscosity. The slowdown in going to Dmim, which is just outside of the error bars, may indicate that the 10 carbon chain slightly rigidifies the packing in the ionic pocket.

The effect of chain length on the second wobbling motion is more substantial. There is a factor of two slowdown in the cone diffusion from $EmimNTf_2$ to $DmimNTf_2$. This is again smaller than the bulk viscosity change and thus is most likely dominated by local effects. For the probe to diffuse beyond the first cone, larger-scale motions of the solvation shell involving the cation are required. These motions are inhibited by the growing alkyl chain length.

The longest time scale is for complete orientational relaxation, reported as τ_m and $1/6D_m$ in the inset in Figure 3. $1/6D_m$ directly tracks the bulk viscosity for $EmimNTf_2$ and $BmimNTf_2$ and can be fixed to the hydrodynamic prediction of eq 16, as discussed above, without compromising the resulting fits to the $HmimNTf_2$ and $DmimNTf_2$ data. The results for $EmimNTf_2$ and $BmimNTf_2$ are consistent with our previous hypothesis in the case of $EmimNTf_2$ that the size and shape of the $SeCN^-$, combined with the nature of its solvation structure, mean that full orientational relaxation is not possible without the cations moving to an extent where the bulk viscosity becomes the dominant factor.

We note that fixing the final reorientation time to the corresponding hydrodynamic predictions for the $HmimNTf_2$ and $DmimNTf_2$ samples is not crucial to any of the trends discussed above.

3.B.2. 2D IR. Figure 4 shows the CLS(T_w) decay curves for both parallel and perpendicular polarization signal pathways of the CN stretch of $SeCN^-$ for the four chain length samples. It is clear that the parallel and perpendicular pathways produce different decays for all four chain lengths. This polarization dependence is due to the effect of RISD[26], as discussed in section 2.C. The differences in the parallel and perpendicular curves reflect the contribution of orientational relaxation to probe frequency fluctuations. The reorientation of the probe in the net electric field produced by the sample at the location of the probe changes the first-order Stark effect interaction, causing spectral shifts. The CLS variable reflects a polarization-weighted FFCF. The FFCF factors into two functions, as in eq 10,[25] the RISD function, giving the contribution of the reorientation-induced frequency fluctuations appropriate for the polarization pathway (eqs 11−13), and the SSD, reflecting the effects of structural changes in the samples sensed by the probe. The RISD factor is completely determined using the PSPP data, as presented in section 3.B, enabling the SSD to be obtained. Because the SSD reflects purely environmental fluctuations, it is not polarization-dependent and is shared in

DOI: 10.1021/acs.jpcb.6b05397
J. Phys. Chem. B 2016, 120, 7488−7501

fitting the two polarizations simultaneously. Knowledge of the RISD term enables a meaningful determination of the SSD.

The SSD is modeled as a sum of exponentials to account for the variety of time scales observed. In the case of the data presented here, a biexponential function is appropriate. A biexponential substantially improves the fits compared to a single exponential, and a triexponential fit is ill-conditioned and does not converge to a result with three distinct time scales. Table 3 gives the results of the biexponential SSD fits to the CLS(T_w) for the four RTILs. The results include the two time constants with their respective amplitudes.

Table 3. Biexponential SSD Parameters

	A_1	t_1(ps)	A_2	t_2(ps)
$EmimNTf_2$	0.30 ± 0.03	8.5 ± 1	0.43 ± 0.03	48 ± 3
$BmimNTf_2$	0.31 ± 0.01	9.4 ± 1	0.50 ± 0.01	81 ± 3
$HmimNTf_2$	0.26 ± 0.01	9.7 ± 1	0.54 ± 0.01	85 ± 3
$DmimNTf_2$	0.22 ± 0.01	8.4 ± 1	0.55 ± 0.01	97 ± 4

To show the differences among the four samples and to test the ability of the RISD model to capture the polarization dependence, the SSD numbers in Table 3 are used in eq 13 to construct the isotropic CLS(T_w). The calculated isotropic curves formed from the SSD parameters obtained from the simultaneous fits to the data for the two polarizations can be compared with the experimental isotropic CLS(T_w) curves that were determined from the isotropic 2D IR spectra, which are the appropriate combinations of the parallel and perpendicular spectra, as in eq 3. To ensure that the experimental parallel and perpendicular spectra have the correct normalization relative to each other, they are separately normalized to the corresponding polarized pump−probe spectra at each time. The projection of the 2D spectrum onto the ω_m axis is the pump−probe spectrum. The parallel and perpendicular pump−probe spectra are acquired such that they have the correct relative amplitudes. The resulting spectra at each T_w were analyzed to yield their CLS curves for the four chain lengths, and those curves are overlaid with the reconstructed CLS curves from eq 13 and our SSD parameters in Figure 5. Only one adjustable parameter was used, which is an offset. As in the anisotropy decays, the offset is required because the polarization dependence of the very slow potassium-influenced ensemble is not accounted for in the reconstructed curves. The comparison between the calculated curves and the experimental data shown in Figure 5 is very good, and it is clear that the RISD framework captures the polarization dependence so that we are confident that the SSD numbers extracted are appropriate.

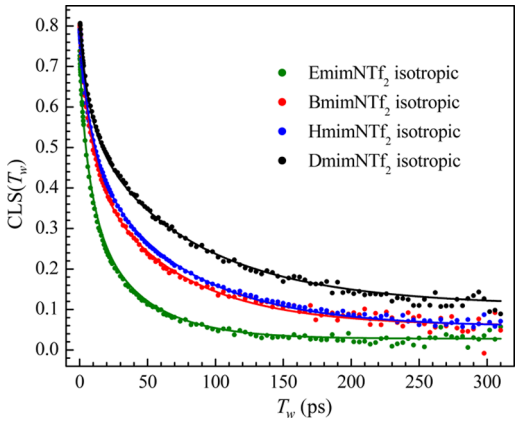

Figure 5. Isotropic CLS curves for the four chain lengths derived from the parallel and perpendicular 2D IR spectra. The overlaid fit is the reconstruction based on eq 13 of the RISD theory. The only free parameter is an overall offset to account for the presence of K^+ ions (see the text).

The short and long time scale SSD decay time constants have different dependences on chain length. The shorter decay time does not change within error for all four chain lengths, whereas the longer decay time exhibits a nonuniform and non-hydrodynamic trend. For this longer decay time, there is a factor of 2 jump going from 2 carbons to 4, but then, the increase becomes gradual going from 4 to 10 carbons. To interpret this behavior, we consider the origin of these decay constants. The structural evolution described by the SSD is modeled in terms of the first-order Stark effect. The correlation function being considered here is the correlation function of the field amplitude and direction of the external electric field that couples to the probe to produce shifts in frequency. Because our probe is an anion that is solvated in the RTIL ionic regions, it is predominantly surrounded by the charged moieties of the RTIL, particularly the positively charged imidazolium rings. Along with the anions present, the solvation pocket attempts to organize in a charge-alternating manner. The field experienced by the probe is the sum of the various fields exerted by these charged moieties in the immediately surrounding ion cluster and also from more distant sources of the electric field. It is likely that the local ionic cluster containing the probe is the dominant source of the electric field experienced by the probe. The portion of the field contributed by the local cluster, in both amplitude and direction, is sensitive to the details of the packing structure and orientation of the imidazolium cations and the NTf_2^- ions.

The existence, then, of a short time scale that is invariant to chain length is a signature of a motion that is small in scale and hence occurs naturally on a fast time scale. The small scale of this motion also means that it can occur without major structural rearrangements or constraint release in the surrounding RTIL alkyl regions. We can therefore interpret the insensitivity to chain length as evidence that the origin of the fast relaxation involves imidazolium motions that do not require significant configurational changes in the alkyl chain arrangements. On its own, the lack of chain length dependence for the short time dynamics would not be enough to guarantee that these motions would not in some manner sense the longer chain length through feedback from the bulk viscosity or altered packing caused by polar−apolar domain growth, for example. The invariance of the shorter decay time is, therefore, an indication that the packing is not altered so fundamentally that these motions differ, consistent with our discussion so far and further indication that the bulk viscosity does not affect smaller fast local motions in these complex liquids.

Following the large change in the slow decay time constant in going from $EmimNTf_2$ to $BmimNtF_2$, the longer decay time's growth is slow past $BmimNTf_2$. The slowdown can be interpreted as motions being on a length scale where at least some require configurational changes on the part of the alkyl chains and may be sensitive to the nature of polar−apolar ordering. The growth of the polar−apolar ordering is generally thought of as gradual, with $BmimNTf_2$ being the threshold case where one can talk about polar−apolar ordering. The trend following $EmimNTf_2$ is consistent with $EmimNTf_2$ not having an apolar moiety of any size that would induce apolar domains

DOI: 10.1021/acs.jpcb.6b05397
J. Phys. Chem. B 2016, 120, 7488−7501

Table 4. Isotropic FFCF Parameters

sample	T_2 (ps)[a]	Γ (cm^{-1})[b]	Δ_1 (cm^{-1})[d]	τ_1 (ps)[c]	Δ_2 (cm^{-1})[d]	τ_2 (ps)[c]	Δ_{off} (cm^{-1})[d]	$fwhm_I$ (cm^{-1})[e]	$fwhm_{tot}$ (cm^{-1})[f]
Emim	2.0 ± 0.1	5.4 ± 0.2	5.3 ± 0.1	5.1 ± 0.3	5.7 ± 0.1	34 ± 2	1.5 ± 0.1	18.8	21.8
Bmim	2.6 ± 0.1	4.2 ± 0.2	5.5 ± 0.2	6.8 ± 0.6	6.2 ± 0.1	59 ± 4	2.3 ± 0.2	20.3	22.6
Hmim	2.5 ± 0.1	4.3 ± 0.2	5.2 ± 0.3	7.1 ± 0.5	6.5 ± 0.1	64 ± 3	2.5 ± 0.1	20.5	22.9
Dmim	2.6 ± 0.1	4.1 ± 0.2	4.8 ± 0.3	10.0 ± 0.6	6.7 ± 0.2	82 ± 4	3.3 ± 0.2	20.9	23.2

[a] T_2: homogeneous dephasing time. [b] Γ: homogeneous line width; fwhm. [c] τ_i: ith component decay constant. [d] Δ_i: ith component inhomogeneous width; standard deviation. [e] $fwhm_I$: inhomogeneous fwhm associated with the total delta, which is the square root of the sum of the squares of the individual Δ_i. [f] $fwhm_{tot}$: overall fwhm including the delta by assuming a Voigt result.[57]

to form by alignment of neighboring cations. Theoretical work has found that the partial charge of the second carbon is not quite what would be expected for alkanes and is still under the influence of the imidazolium ring.[51] This line of reasoning suggests a somewhat fundamental change in behavior going from two carbons to four. At four carbons, a large enough hydrophobic moiety exists that a hydrophobic effect comes into play driving cations to arrange themselves such that the hydrophobic chains can cluster, in other words, so that apolar domains exist. The existence of a potential favoring alignment directly implies that the cations are no longer as free to reorient because reorientation now requires disruption of the apolar ordering. Moreover, $Bmim^+$ and the longer chain length cations are significantly more elongated and asymmetric, resulting in a greater steric barrier to complete orientational randomization compared to $Emim^+$. This reasoning therefore suggests that motions, which are possible in the ethyl case, are no longer accessible or are significantly slowed down to a degree that eliminates their contribution to the observed long time scale decay starting with $Bmim^+$.

In addition to the RISD analysis above, the experimentally derived isotropic CLS curves in Figure 5 can be fit as a sum of exponentials. This analysis makes no assumptions on the origin or nature of the motions contributing to spectral diffusion and is therefore a more general benchmark, which is useful for comparison to simulation or other measurements that do not separate SSD and RISD. We fit the four isotropic CLS curves in Figure 5 (fits not shown) to the form in eq 8 with one motionally narrowed component and two exponentials. As discussed in section 2.B, the CLS(T_w) decay is the normalized version of the FFCF and can be combined with the FT-IR spectrum to yield the full FFCF with spectral fluctuation amplitudes Δ_i, the total homogeneous line width Γ, and the time constants. The results of this analysis are given in Table 4.

3.B.3. OHD-OKE. OHD-OKE data were measured for the four neat ionic liquids as well as $EmimNTf_2$, $BmimNTf_2$, and $HmimNTf_2$ with $SeCN^-$ at the same concentration as that in the IR experiments. Figure 6 shows the OHD-OKE data for the four neat liquids. Note the logarithmic axes and that the data have been vertically offset for clarity. The data for the doped ionic liquids look identical within experimental error, which demonstrates that adding low-concentration KSeCN does not change the bulk liquid dynamics.

Each of the seven decays was fit using eq 14 from 1 ps to near the end of the exponential decay. Neither power law exponent showed a trend with increasing chain length, which suggests that the increasing size of the nonpolar alkyl region does not affect the short time nondiffusive caged motions of the ions. Additionally, there was not a significant change in the power laws for the doped samples relative to the neat. This suggests that the $SeCN^-$ probe is not disturbing the fast, short-range motions of the molecules and that it is an appropriate

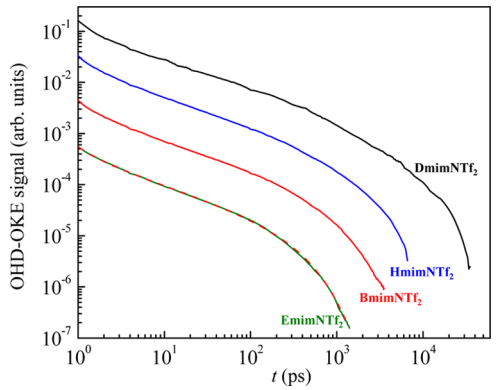

Figure 6. OHD-OKE data for the four neat ionic liquids. Data have been vertically offset for clarity. All data sets were fit using eq 14. A sample fit to $EmimNTf_2$ data is shown as the red dashed line. Fits for the other neat liquids and all of the doped liquids were of similar quality.

choice of probe to monitor dynamics in the IR without changing the fundamental nature of the liquid dynamics. The dopant independence of the caged motions is in agreement with previous OHD-OKE studies of small concentrations of dopants in liquid crystals and ordinary liquids.[52,53] The average value of z for the samples was 2.26 ± 0.27, and the average value of b was 0.41 ± 0.02. These numbers match those from previous OHD-OKE temperature studies of neat $BmimNTf_2$ within experimental error.[54]

The final exponential time constants, τ, are reported in Table 5. The time constant increases as the chain length and viscosity

Table 5. OHD-OKE Final Exponential Time Constants

sample		τ (ps)
$EmimNTf_2$	neat	383 ± 10
	doped	394 ± 10
$BmimNTf_2$	neat	1091 ± 10
	doped	1078 ± 10
$HmimNTf_2$	neat	1938 ± 10
	doped	1956 ± 10
$DmimNTf_2$	neat	4820 ± 80

increase. For all four ionic liquids, the time scales reported in the OHD-OKE experiments are much slower than any time scale measured in the IR experiments. The OHD-OKE measured time constant is for complete orientational relaxation of the liquid. The liquid will not be able to undergo complete orientational randomization without randomizing the entire liquid structure. Therefore, complete spectral diffusion, that is, randomization of all structures that contribute to inhomogeneous broadening of the CN stretch vibrational spectrum, does

DOI: 10.1021/acs.jpcb.6b05397
J. Phys. Chem. B 2016, 120, 7488−7501

not require complete randomization of the bulk liquid structure.

Returning to the K^+-induced offsets observed in the anisotropy data, it is reasonable to address two possibilities that might account for the increased offset with increased chain length. The effect could be due to a small population of $SeCN^-$ contained in a K^+-induced cluster of the RTIL cations and anions. Selenocyanates in these clusters experience much slower dynamics than those in the bulk that are not influenced by potassium. The increasing offsets indicate an increase in the fraction of $SeCN^-$ that is affected by the presence of potassium. Because the concentration of potassium ions is the same for all samples, two scenarios are plausible. In the first scenario, there is no specific interaction between the potassium cluster and the $SeCN^-$. The potassium organizes the ionic liquid in a manner that restricts the motions that are responsible for the dynamics in the bulk liquid that give rise to the $SeCN^-$ time-dependent observables. If the volume of the K^+ clusters increases, then statistically more $SeCN^-$ ions will be affected. This scenario requires a mechanism for the growth in size of the K^+ clusters with chain length. Because the potassium will be mainly surrounded by anions,[55] it is not likely that an increase in chain length, which places restrictions on imidazolium's configurations relative to the NTf_2 anions, would lead to larger solvation clusters around the K^+ ions.

The second and possibly more plausible scenario is that there is an equilibrium process governing the association of the $SeCN^-$ ions with the potassium clusters. Because K^+ is believed to form a cage of anions by outcompeting the RTIL cations, it can also presumably outcompete the native RTIL cations for the $SeCN^-$ ion to some extent. If the dynamics within the solvation shell of the potassium are substantially slowed compared to the bulk RTIL dynamics, then the $SeCN^-$ in that shell will exhibit a significant slowing down in its relaxation processes. The increasing offsets with chain length can be caused by an increase in the equilibrium constant for the preference of $SeCN^-$ to be in K^+ clusters rather than in the bulk RTIL. The result is larger offsets in the PSPP and 2D IR data with increasing chain length.

3.C. Discussion. In section 3, we have presented the details resulting from the absorption spectra and three time-resolved measurements. A coherent picture of the structure and dynamics of the RTILs as reported by the $SeCN^-$ emerges. The first observation is that the similarity in the FT-IR spectra and the vibrational lifetimes indicate that the chemical environment, in terms of the solvation interactions exerted, their effect on probe−solvent coupling, and the available relaxation pathways, is very similar in all four chain lengths. The small differences in the spectrum with increasing chain length show that there are small changes in the structural arrangement of the ions surrounding the $SeCN^-$, but these are not sufficient to change the coupling pathways for vibrational relaxation of the CN stretch. The driving force for polar−apolar ordering is to avoid having the hydrophobic alkyl chain interrupt the charge alternation within the ionic regions. The ionic regions in the long alkyl chain RTILs seek to conserve the same ionic region structures that confer stability in the case of $EmimNTf_2$. That the FT-IR spectra show some broadening and red shift with increasing alkyl chain length suggests that there is some trade-off between accommodating ion−ion interactions and the alkyl chain interactions.

That the ion packing is little changed with increasing chain length is also supported by the observed lack of a trend in the reorientational cone angles. The cone angles, which result from structural restrictions on reorientation, are the most directly tied to the topography of the packing. The most likely scenario then is that there are additional structures that arise with increasing alkyl chain length. These additional structures, or even just the increasing apolar separation between adjacent polar domains, combine to create more inhomogeneity in the overall solvation environment, including long-range interactions, experienced by the probe molecule, consistent with the slight broadening observed in the FT-IR. The existence of an interface with apolar domains exposes a fraction of the probe molecules to lower electric fields than otherwise present with shorter alkyl chains, producing the observed FT-IR red shift. The relative invariance of the cone angles shows that these changes do not fundamentally change the ion packing experienced by the vast majority of the $SeCN^-$ anions. Because the $SeCN^-$ anions remain solvated by imidazolium cations, the size and shape of the imidazolium, combined with the specific nature of these interactions, dominate the orientational restrictions in the absence of fundamental changes in the packing structure of the ionic regions.

The observed sensitivity of the observed dynamics to chain length depends on the extent and nature of the medium's motions. There are many kinds of motions involved in orientational constraint release or structural fluctuations that give rise to SSD. These motions include very small ballistic translations and orientational wobbling about various axes, cation configurational changes, diffusive translations, solvation shell number changes, and overall orientational relaxation. In the case of orientational restrictions, the ballistic cone relaxation requires only the smallest scale motions. This solvent cage determines the first diffusive cone time scale during which the restrictions are those that cannot be lifted by motions of the same time scale. The same reasoning then produces the second diffusive cone where the motions required to escape the restriction are so large that the motions that they require disturb the ionic pocket to an extent that the bulk viscosity determines the overall orientational diffusion. These are the largest scale motions that are necessary for the $SeCN^-$ to experience the full range of dynamics that it reports on through the IR observables.

The frequency fluctuations of the probe (SSD), as distinct from its orientational relaxation, are mainly sensitive to fluctuations of the surrounding ions. The complete invariance of the first time scale to chain length suggests that they involve small-scale fluctuations of the imidazolium that do not involve alkyl chain structural changes. The importance of the role played by the imidazolium is further supported by the jump observed going from $EmimNTf_2$ to $BmimNTf_2$ in the second SSD time scale, suggesting movements of the imidazolium that are restricted by the presence of the alkyl chain and its affinity for apolar segregation.

It is notable that all of the orientational relaxation of the $SeCN^-$ and the SSD that it reports occur much faster than the complete relaxation of the RTIL measured with the OHD-OKE experiments. The slowest time scale considered, which is the overall orientational relaxation of the $SeCN^-$, is more than 4 times faster in $EmimNTf_2$ than the overall orientational randomization of RTIL. This factor increases to 15-fold in the case of $DmimNTf_2$. If even the slowest time scale of the probe, the one sensitive to bulk properties like viscosity, is still much faster than overall relaxation of the ionic liquid, then it is

DOI: 10.1021/acs.jpcb.6b05397
J. Phys. Chem. B 2016, 120, 7488−7501

clear that local motions and limited motions play a very important role in the solvation dynamics.

4. CONCLUDING REMARKS

The dynamics and structure of four $C_n$mimNTf$_2$ RTILs were investigated as a function of the alkyl chain length using a linear anion, $SeCN^-$, as a vibrational probe. FT-IR experiments and vibrational lifetime measurements on the CN stretch were used to gain insight into the effect of chain length on the structure of the ionic regions present in these RTILs. The results showed that increasing chain length caused a relatively small change in the structure of the ionic regions. The vibrational lifetimes, which are sensitive to the interactions of the probe with its immediate environment, were independent of chain length within experimental error. The absorption spectrum shifted slightly to lower frequency and broadened a small amount as the chain length increased, which indicates some degree of structural modification with increasing chain length.

The anisotropy decays, measured with PSPP experiments and analyzed through a hierarchical wobbling-in-a-cone model, provided detailed information on the orientational motion of the probe. These measurements provide information on RTIL constraints on the probe reorientation and the time scales on which restrictions are overcome. While complete orientational relaxation was found to be hydrodynamic, all of the shorter time scale relaxations are much less affected by the bulk viscosity. This is the result of the local nature of the motions involved, which do not involve the bulk IL structure to the extent that the bulk viscosity becomes relevant.

The spectral fluctuations of the probe vibration were characterized with 2D IR. The spectral diffusion resulted from fluctuations of the solvent environment and was separated from the RISD. The resulting SSD did not scale simply with viscosity. While the faster motions are invariant to chain length, a reflection of their limited extent and local nature, the slower motions were found to depend on chain length in a discontinuous manner. Specifically, a substantial slowing was found going from two carbons to four carbons in the alkyl chain. This slowdown is attributed to new restrictions on imidazolium motions due to the presence of a hydrophobic alkyl chain, which gives rise to apolar regions. The additional slowing in going to even longer chains was mild. Chain entanglement in the apolar regions, which increases with chain length, affects the fast structural fluctuations of the ions.

All of the dynamics observed for the probe occur on a much faster time scale than the overall orientational relaxation of the RTILs measured through OHD-OKE. This reinforces the results that show that overall structural relaxation of the RTIL is not required for most of the local anion observables to entirely relax. The overall picture that emerges is that of complex layers of structure and dynamics that arise from the spatial heterogeneity. This picture needs to be considered when interpreting observations of bulk ILs and when optimizing their properties for specific applications. The structure−function link in ILs is known to be frequently counterintuitive. Predictions of microscopic influences on bulk behavior, such as the effect of hydrogen bonding on viscosity[50,56] or the results of adding water,[35,49] are difficult. Reasoning from bulk also fails to predict properties, like conductivity,[55] which are critical for certain applications. Because many applications involve local structure and dynamics or, like conductivity, are intimately tied to local effects, exploring the links between composition, ordering, structure, and dynamics is a necessary step for successful applications and for the identification of the structural handles and tuning parameters that may mitigate impediments to applications.

■ ASSOCIATED CONTENT

Supporting Information

The Supporting Information is available free of charge on the ACS Publications website at DOI: 10.1021/acs.jpcb.6b05397.

Results of free triexponential fits to the anisotropy curves, a discussion of the effect of the potassium-induced offset on the wobbling-in-a-cone analysis, and viscosity measurements for the four ionic liquids studied in this work (PDF)

■ AUTHOR INFORMATION

Corresponding Author

*E-mail: fayer@stanford.edu.

Notes

The authors declare no competing financial interest.

■ ACKNOWLEDGMENTS

We thank Patrick L. Kramer, Jun Nishida, and Chiara H. Giammanco for helpful discussions and Steven A. Yamada for experimental assistance. We also thank Adam L. Sturlaugson for having synthesized the EmimSeCN used in this and previous work. This material is based on work supported by the Air Force Office of Scientific Research under AFOSR Award Number FA9550-16-1-0104 (A.T. and M.D.F), and the Division of Chemistry, Directorate of Mathematical and Physical Sciences, National Science Foundation (NSF) (CHE-1461477) (H.E.B. and M.D.F.).

■ REFERENCES

(1) Castner, E. W.; Margulis, C. J.; Maroncelli, M.; Wishart, J. F. Ionic Liquids: Structure and Photochemical Reactions. *Annu. Rev. Phys. Chem.* **2011**, *62*, 85−105.

(2) Hayes, R.; Warr, G. G.; Atkin, R. Structure and Nanostructure in Ionic Liquids. *Chem. Rev.* **2015**, *115*, 6357−6426.

(3) Garcia, B.; Lavallée, S.; Perron, G.; Michot, C.; Armand, M. Room Temperature Molten Salts as Lithium Battery Electrolyte. *Electrochim. Acta* **2004**, *49*, 4583−4588.

(4) Del Pópolo, M. G.; Voth, G. A. On the Structure and Dynamics of Ionic Liquids. *J. Phys. Chem. B* **2004**, *108*, 1744−1752.

(5) Wang, Y.; Jiang, W.; Yan, T.; Voth, G. A. Understanding Ionic Liquids through Atomistic and Coarse-Grained Molecular Dynamics Simulations. *Acc. Chem. Res.* **2007**, *40*, 1193−1199.

(6) Canongia Lopes, J. N. A.; Pádua, A. A. H. Nanostructural Organization in Ionic Liquids. *J. Phys. Chem. B* **2006**, *110*, 3330−3335.

(7) Triolo, A.; Russina, O.; Bleif, H.-J.; Di Cola, E. Nanoscale Segregation in Room Temperature Ionic Liquids†. *J. Phys. Chem. B* **2007**, *111*, 4641−4644.

(8) Triolo, A.; Russina, O.; Fazio, B.; Triolo, R.; Di Cola, E. Morphology of 1-Alkyl-3-Methylimidazolium Hexafluorophosphate Room Temperature Ionic Liquids. *Chem. Phys. Lett.* **2008**, *457*, 362−365.

(9) Russina, O.; Triolo, A.; Gontrani, L.; Caminiti, R.; Xiao, D.; Hines, L. G., Jr.; Bartsch, R. A.; Quitevis, E. L.; Pleckhova, N. V.; Seddon, K. R. Morphology and Intermolecular Dynamics of 1-Alkyl-3-Methylimidazolium Bis{(Trifluoromethane)Sulfonyl}Amide Ionic Liquids: Structural and Dynamic Evidence of Nanoscale Segregation. *J. Phys.: Condens. Matter* **2009**, *21*, 424121.

(10) Hardacre, C.; Holbrey, J. D.; Mullan, C. L.; Youngs, T. G. A.; Bowron, D. T. Small Angle Neutron Scattering from 1-Alkyl-3-Methylimidazolium Hexafluorophosphate Ionic Liquids ([Cnmim][Pf6], N = 4, 6, and 8). *J. Chem. Phys.* **2010**, *133*, 074510.

DOI: 10.1021/acs.jpcb.6b05397
J. Phys. Chem. B 2016, 120, 7488−7501

(11) Fruchey, K.; Fayer, M. D. Dynamics in Organic Ionic Liquids in Distinct Regions Using Charged and Uncharged Orientational Relaxation Probes. *J. Phys. Chem. B* **2010**, *114*, 2840−2845.
(12) Wang, C. C.; Pecora, R. Time-Correlation Functions for Restricted Rotational Diffusion. *J. Chem. Phys.* **1980**, *72*, 5333−5340.
(13) Lipari, G.; Szabo, A. Effect of Librational Motion on Fluorescence Depolarization and Nuclear Magnetic-Resonance Relaxation in Macromolecules and Membranes. *Biophys. J.* **1980**, *30*, 489−506.
(14) Lipari, G.; Szabo, A. Model-Free Approach to the Interpretation of Nuclear Magnetic-Resonance Relaxation in Macromolecules 0.1. Theory and Range of Validity. *J. Am. Chem. Soc.* **1982**, *104*, 4546−4559.
(15) Tan, H.-S.; Piletic, I. R.; Fayer, M. D. Orientational Dynamics of Water Confined on a Nanometer Length Scale in Reverse Micelles. *J. Chem. Phys.* **2005**, *122*, 174501.
(16) Kramer, P. L.; Giammanco, C. H.; Fayer, M. D. Dynamics of Water, Methanol, and Ethanol in a Room Temperature Ionic Liquid. *J. Chem. Phys.* **2015**, *142*, 212408.
(17) Kinosita, K.; Kawato, S.; Ikegami, A. Theory of Fluorescence Polarization Decay in Membranes. *Biophys. J.* **1977**, *20*, 289−305.
(18) Kinosita, K.; Ikegami, A.; Kawato, S. On the Wobbling-in-Cone Analysis of Fluorescence Anisotropy Decay. *Biophys. J.* **1982**, *37*, 461−464.
(19) Araque, J. C.; Daly, R. P.; Margulis, C. J. A Link between Structure, Diffusion and Rotations of Hydrogen Bonding Tracers in Ionic Liquids. *J. Chem. Phys.* **2016**, *144*, 204504.
(20) Karthick Kumar, S. K.; Tamimi, A.; Fayer, M. D. Comparisons of 2d Ir Measured Spectral Diffusion in Rotating Frames Using Pulse Shaping and in the Stationary Frame Using the Standard Method. *J. Chem. Phys.* **2012**, *137*, 184201.
(21) Tokmakoff, A. Orientational Correlation Functions and Polarization Selectivity for Nonlinear Spectroscopy of Isotropic Media. 1. Third Order. *J. Chem. Phys.* **1996**, *105*, 1−12.
(22) Moilanen, D. E.; Fenn, E. E.; Lin, Y. S.; Skinner, J. L.; Bagchi, B.; Fayer, M. D. Water Inertial Reorientation: Hydrogen Bond Strength and the Angular Potential. *Proc. Natl. Acad. Sci. U. S. A.* **2008**, *105*, 5295−5300.
(23) Fenn, E. E.; Wong, D. B.; Fayer, M. D. Water Dynamics in Small Reverse Micelles in Two Solvents: Two-Dimensional Infrared Vibrational Echoes with Two-Dimensional Background Subtraction. *J. Chem. Phys.* **2011**, *134*, 054512.
(24) Park, S.; Kwak, K.; Fayer, M. D. Ultrafast 2d-Ir Vibrational Echo Spectroscopy: A Probe of Molecular Dynamics. *Laser Phys. Lett.* **2007**, *4*, 704−718.
(25) Kramer, P. L.; Nishida, J.; Fayer, M. D. Separation of Experimental 2d Ir Frequency-Frequency Correlation Functions into Structural and Reorientation-Induced Contributions. *J. Chem. Phys.* **2015**, *143*, 124505.
(26) Kramer, P. L.; Nishida, J.; Giammanco, C. H.; Tamimi, A.; Fayer, M. D. Observation and Theory of Reorientation-Induced Spectral Diffusion in Polarization-Selective 2d Ir Spectroscopy. *J. Chem. Phys.* **2015**, *142*, 184505.
(27) Hamm, P.; Zanni, M. T. *Concepts and Methods of 2D Infrared Spectroscopy*; Cambridge University Press: Cambridge; New York, 2011.
(28) Kwak, K.; Park, S.; Finkelstein, I. J.; Fayer, M. D. Frequency-Frequency Correlation Functions and Apodization in 2d-Ir Vibrational Echo Spectroscopy, a New Approach. *J. Chem. Phys.* **2007**, *127*, 124503.
(29) Kwak, K.; Rosenfeld, D. E.; Fayer, M. D. Taking Apart the Two-Dimensional Infrared Vibrational Echo Spectra: More Information and Elimination of Distortions. *J. Chem. Phys.* **2008**, *128*, 204505.
(30) Smith, N. A.; Meech, S. R. Optically-Heterodyne-Detected Optical Kerr Effect (Ohd-Oke): Applications in Condensed Phase Dynamics. *Int. Rev. Phys. Chem.* **2002**, *21*, 75−100.
(31) Kinoshita, S.; Sakai, Y.; Miyazaki, J.; Watanabe, J. Fundamental Aspects of Light Scattering and Optical Kerr Effect Spectroscopy. *Eur. Phys. J.: Spec. Top.* **2012**, *209*, 1−100.
(32) McMorrow, D.; Lotshaw, W. T. Intermolecular Dynamics in Acetonitrile Probed with Femtosecond Fourier Transform Raman Spectroscopy. *J. Phys. Chem.* **1991**, *95*, 10395−10406.
(33) McMorrow, D.; Lotshaw, W. T.; Kenney-Wallace, G. A. Femtosecond Optical Kerr Studies on the Origin of the Nonlinear Response in Simple Liquids. *IEEE J. Quantum Electron.* **1988**, *24*, 443−454.
(34) Sturlaugson, A. L.; Fruchey, K. S.; Fayer, M. D. Orientational Dynamics of Room Temperature Ionic Liquid/Water Mixtures: Evidence for Water-Induced Structure and Anisotropic Cation Solvation. *J. Phys. Chem. B* **2012**, *116*, 1777−1787.
(35) Sturlaugson, A. L.; Arima, A. Y.; Bailey, H. E.; Fayer, M. D. Orientational Dynamics in a Lyotropic Room Temperature Ionic Liquid. *J. Phys. Chem. B* **2013**, *117*, 14775−14784.
(36) Sturlaugson, A. L.; Fruchey, K. S.; Lynch, S. R.; Aragon, S. R.; Fayer, M. D. Orientational and Translational Dynamics of Polyether/Water Solutions. *J. Phys. Chem. B* **2010**, *114*, 5350−5358.
(37) Cang, H.; Li, J.; Fayer, M. D. Orientational Dynamics of the Ionic Organics Liquid 1-Ethyl-3-Methylimidazolium Nitrate. *J. Chem. Phys.* **2003**, *119*, 13017−13023.
(38) Cang, H.; Li, J.; Novikov, V. N.; Fayer, M. D. Dynamics in Supercooled Liquids and in the Isotropic Phase of Liquid Crystals: A Comparison. *J. Chem. Phys.* **2003**, *118*, 9303−9311.
(39) Cang, H.; Novikov, V. N.; Fayer, M. D. Logarithmic Decay of the Orientational Correlation Function in Supercooled Liquids on the Ps to Ns Time Scale. *J. Chem. Phys.* **2003**, *118*, 2800−2807.
(40) Li, J.; Cang, H.; Andersen, H. C.; Fayer, M. D. A Mode Coupling Theory Description of the Short- and Long-Time Dynamics of Nematogens in the Isotropic Phase. *J. Chem. Phys.* **2006**, *124*, 014902.
(41) Tamimi, A.; Fayer, M. D. Ionic Liquid Dynamics Measured with 2D IR and IR Pump−Probe Experiments on a Linear Anion and the Influence of Potassium Cations. *J. Phys. Chem. B* **2016**, *120*, 5842.
(42) Yuan, R.; Yan, C.; Tamimi, A.; Fayer, M. D. Molecular Anion Hydrogen Bonding Dynamics in Aqueous Solution. *J. Phys. Chem. B* **2015**, *119*, 13407−13415.
(43) Annapureddy, H. V. R.; Kashyap, H. K.; De Biase, P. M.; Margulis, C. J. What Is the Origin of the Prepeak in the X-Ray Scattering of Imidazolium-Based Room-Temperature Ionic Liquids? *J. Phys. Chem. B* **2010**, *114*, 16838−16846.
(44) Russina, O.; Triolo, A.; Gontrani, L.; Caminiti, R. Mesoscopic Structural Heterogeneities in Room-Temperature Ionic Liquids. *J. Phys. Chem. Lett.* **2012**, *3*, 27−33.
(45) Moog, R. S.; Ediger, M. D.; Boxer, S. G.; Fayer, M. D. Viscosity Dependence of the Rotational Reorientation of Rhodamine B in Mono- and Polyalcohol. Picosecond Transient Grating Experiments. *J. Phys. Chem.* **1982**, *86*, 4694−4700.
(46) Youngren, G. K.; Acrivos, A. Rotational Friction Coefficients for Ellipsoids and Chemical Molecules with the Slip Boundary Condition. *J. Chem. Phys.* **1975**, *63*, 3846−3849.
(47) Hu, C.-M.; Zwanzig, R. Rotational Friction Coefficients for Spheroids with the Slipping Boundary Condition. *J. Chem. Phys.* **1974**, *60*, 4354−4357.
(48) Sension, R. J.; Hochstrasser, R. M. Comment On: Rotational Friction Coefficients for Ellipsoids and Chemical Molecules with Slip Boundary Conditions. *J. Chem. Phys.* **1993**, *98*, 2490−2490.
(49) Seddon, K. R.; Stark, A.; Torres, M.-J. Influence of Chloride, Water, and Organic Solvents on the Physical Properties of Ionic Liquids. *Pure Appl. Chem.* **2000**, *72*, 2275−2287.
(50) Bonhôte, P.; Dias, A.-P.; Papageorgiou, N.; Kalyanasundaram, K.; Grätzel, M. Hydrophobic, Highly Conductive Ambient-Temperature Molten Salts. *Inorg. Chem.* **1996**, *35*, 1168−1178.
(51) Canongia Lopes, J. N.; Deschamps, J.; Pádua, A. A. H. Modeling Ionic Liquids Using a Systematic All-Atom Force Field. *J. Phys. Chem. B* **2004**, *108*, 2038−2047.
(52) Sokolowsky, K. P.; Bailey, H. E.; Fayer, M. D. New Divergent Dynamics in the Isotropic to Nematic Phase Transition of Liquid Crystals Measured with 2d Ir Vibrational Echo Spectroscopy. *J. Chem. Phys.* **2014**, *141*, 194502.

DOI: 10.1021/acs.jpcb.6b05397
J. Phys. Chem. B 2016, 120, 7488−7501

(53) Sokolowsky, K. P.; Bailey, H. E.; Fayer, M. D. Length Scales and Structural Dynamics in Nematogen Pseudonematic Domains Measured with 2d Ir Vibrational Echoes and Optical Kerr Effect Experiments. *J. Phys. Chem. B* **2014**, *118*, 7856−7868.
(54) Nicolau, B. G.; Sturlaugson, A.; Fruchey, K.; Ribeiro, M. C. C.; Fayer, M. D. Room Temperature Ionic Liquid-Lithium Salt Mixtures: Optical Kerr Effect Dynamical Measurements. *J. Phys. Chem. B* **2010**, *114*, 8350−8356.
(55) Tucker, T. G.; Angell, C. A. Approaches to, and Problems with, Ionic Liquid Electrolytes for Alkali Metal Electrochemical Devices: The Case of Low-Melting Chloroaluminate Binary Solutions. *J. Electrochem. Soc.* **2014**, *161*, H796−H801.
(56) Ren, Z.; Ivanova, A. S.; Couchot-Vore, D.; Garrett-Roe, S. Ultrafast Structure and Dynamics in Ionic Liquids: 2d-Ir Spectroscopy Probes the Molecular Origin of Viscosity. *J. Phys. Chem. Lett.* **2014**, *5*, 1541−1546.
(57) Olivero, J. J.; Longbothum, R. L. Empirical Fits to the Voigt Line Width: A Brief Review. *J. Quant. Spectrosc. Radiat. Transfer* **1977**, *17*, 233−236.

DOI: 10.1021/acs.jpcb.6b05397
J. Phys. Chem. B 2016, 120, 7488−7501